

## Analysis of banded microstructures in multiphase steels assisted by transformation-induced plasticity

**Citation for published version (APA):**

Yadegari, S., Turteltaub, S. R., Suiker, A. S. J., & Kok, P. J. J. (2014). Analysis of banded microstructures in multiphase steels assisted by transformation-induced plasticity. *Computational Materials Science*, 84, 339-349. <https://doi.org/10.1016/j.commatsci.2013.12.002>

**DOI:**

[10.1016/j.commatsci.2013.12.002](https://doi.org/10.1016/j.commatsci.2013.12.002)

**Document status and date:**

Published: 01/01/2014

**Document Version:**

Publisher's PDF, also known as Version of Record (includes final page, issue and volume numbers)

**Please check the document version of this publication:**

- A submitted manuscript is the version of the article upon submission and before peer-review. There can be important differences between the submitted version and the official published version of record. People interested in the research are advised to contact the author for the final version of the publication, or visit the DOI to the publisher's website.
- The final author version and the galley proof are versions of the publication after peer review.
- The final published version features the final layout of the paper including the volume, issue and page numbers.

[Link to publication](#)

**General rights**

Copyright and moral rights for the publications made accessible in the public portal are retained by the authors and/or other copyright owners and it is a condition of accessing publications that users recognise and abide by the legal requirements associated with these rights.

- Users may download and print one copy of any publication from the public portal for the purpose of private study or research.
- You may not further distribute the material or use it for any profit-making activity or commercial gain
- You may freely distribute the URL identifying the publication in the public portal.

If the publication is distributed under the terms of Article 25fa of the Dutch Copyright Act, indicated by the "Taverne" license above, please follow below link for the End User Agreement:

[www.tue.nl/taverne](http://www.tue.nl/taverne)

**Take down policy**

If you believe that this document breaches copyright please contact us at:

[openaccess@tue.nl](mailto:openaccess@tue.nl)

providing details and we will investigate your claim.



# Analysis of banded microstructures in multiphase steels assisted by transformation-induced plasticity



S. Yadegari<sup>a</sup>, S. Turteltaub<sup>a,\*</sup>, A.S.J. Suiker<sup>b</sup>, P.J.J. Kok<sup>c</sup>

<sup>a</sup> Faculty of Aerospace Engineering, Delft University of Technology, P.O. Box 5058, 2600 GB Delft, The Netherlands

<sup>b</sup> Department of the Built Environment, Eindhoven University of Technology, P.O. Box 513, 5600 MB Eindhoven, The Netherlands

<sup>c</sup> Tata Steel Research and Development, P.O. Box 10000, 1970 CA IJmuiden, The Netherlands

## ARTICLE INFO

### Article history:

Received 15 May 2013

Received in revised form 19 October 2013

Accepted 2 December 2013

### Keywords:

TRIP steel

Multilevel non-convex Voronoi tessellation

Numerical homogenization

Non-redundant periodic boundary

conditions

Banded microstructures

## ABSTRACT

The influence of the spatial distribution of the austenitic phase on the effective mechanical properties of a multiphase steel assisted by transformation-induced plasticity is analyzed using a numerical homogenization scheme. Representative three-dimensional volume elements with distinct microstructures are created applying a newly-developed algorithm based on the generation of a multilevel Voronoi tessellation; this approach allows for straightforwardly incorporating grains with complex, non-convex shapes in the microstructure. The effective macroscopic response of the samples is computed under the formulation of a set of non-redundant, periodic boundary conditions, which warrants a consistent transition between the microscopic and macroscopic scales. A sample in which austenitic grains are clustered within a ferritic matrix by means of a band-like region is compared to a sample with austenitic grains being randomly dispersed within the ferritic matrix. It is found that the banded microstructure may be detrimental in comparison to the dispersed microstructure, since it allows substantial plastic localization to occur in the ferritic matrix, which in turn diminishes the strengthening effect provided by the austenitic phase.

© 2013 Elsevier B.V. All rights reserved.

## 1. Introduction

A thorough understanding of the link between the microstructural characteristics of a heterogeneous multiphase material and its macroscale response is critical for the enhancement of its mechanical properties. A specific class of technologically-important multiphase materials are those assisted by the transformation-induced plasticity mechanism. This class of steels, commonly referred to as TRIP steels, are characterized by a microstructure containing ferrite as the most dominant phase, complemented by retained austenite, bainite, and occasionally a small amount of thermal martensite, see e.g., [1–7]. The key constituent for steels assisted by transformation-induced plasticity is the retained austenite, which is metastable at room temperature, but may transform into martensite under the application of mechanical and/or thermal loading. The transformation process increases the effective strength of the steel, since the martensitic product phase is significantly harder than the austenitic parent phase and the ferrite-based matrix. It further increases the ductility of the steel, due to plastic deformations induced in the ferritic and bainitic phases by a volumetric expansion of the transforming

austenitic phase. These two microstructural mechanisms essentially characterize the TRIP-effect, and therefore have been taken into account in various macroscopic and microscopic continuum models developed during the last four decades [8–23].

The microstructure of a multiphase steel can be modified by changing its processing route [24,25]. For TRIP steels this may significantly improve the effective material properties, since specific microstructural characteristics, such as the initial volume fraction of austenite, the carbon concentration in the retained austenite, and the crystallographic texture, appear to substantially influence the stability of the retained austenite, and, consequently, the overall mechanical response [26]. The grain size also affects the macroscopic properties, as analyzed in detail by means of both continuum models and discrete models [27,28].

Although the macroscopic properties of a multiphase steel clearly show a dependency on the initial volume fraction of austenite, it is not yet well understood how the *spatial distribution* of the austenite grains contributes to this aspect. For this purpose, two distinct, technologically-relevant microstructural morphologies are analyzed and compared in the present communication, namely (i) a benchmark microstructure with isolated, randomly-distributed austenitic grains embedded in a ferritic matrix and (ii) a microstructure where austenitic grains are clustered in a plate-like region (or band) within a ferritic matrix. The benchmark distribution is typically encountered in cold-rolled TRIP steels that are

\* Corresponding author. Tel.: +31 152785360.

E-mail addresses: [S.Yadegari@tudelft.nl](mailto:S.Yadegari@tudelft.nl) (S. Yadegari), [S.R.Turteltaub@tudelft.nl](mailto:S.R.Turteltaub@tudelft.nl) (S. Turteltaub), [A.S.J.Suiker@tue.nl](mailto:A.S.J.Suiker@tue.nl) (A.S.J. Suiker), [Piet.Kok@tatasteel.com](mailto:Piet.Kok@tatasteel.com) (P.J.J. Kok).

subsequently subjected to a two-step annealing (intercritical annealing followed by isothermal heat treatment), where retained austenite appears in grains wedged between ferritic grains. Conversely, austenitic grains clustered in a band-like region may appear during hot-rolling (i.e., high-temperature mechanical deformation during processing), whenever the banded morphology is not completely removed during further heat treatment, see [29]. The relevance of banded morphologies on the mechanical response of ferrous alloys has been discussed in [30–32]. Their effect on the effective strength was analyzed in [33] by means of a discrete dislocation-transformation model, where it was found that a microstructure composed of randomly-distributed grains of austenite is advantageous, as it delays the onset of plastic localization in comparison to banded microstructures. The present study is based upon a continuum approach which, compared with the above-mentioned discrete model, allows to extend the analysis to a three-dimensional setting as well as to a larger range of deformations, i.e., beyond the onset of plastic deformation. Accordingly, a more comprehensive insight is obtained into the strengthening effect caused by the austenitic phase and the role played by its spatial distribution.

In order to establish a direct link between the spatial distribution of austenite and the macroscopic properties of a multiphase steel, simulations are conducted on banded and dispersed microstructures while keeping all other relevant microstructural features the same (i.e., initial volume fraction of austenite, average crystallographic orientation, carbon content, etc.). The constitutive models used for ferrite and austenite are summarized in Section 2. A multilevel Voronoi algorithm for generating microstructural computational samples of an aggregate of grains is presented in Section 3. The samples are subjected to non-redundant, periodic boundary conditions, which warrants a consistent transition between the microscopic and macroscopic scales. The samples are used in a convergence analysis to establish the required size of a representative volume element for the determination of the macroscopic properties. The effect of a banded microstructure is analyzed in Section 4 based on a comparison with benchmark simulations for dispersed microstructures. Conclusive remarks are provided in Section 5.

## 2. Micromechanical modeling of multiphase TRIP steels

The microstructures considered in the present analysis consist of an aggregate of ferritic grains (primary phase) and metastable retained austenitic grains (secondary phase). Upon loading, the austenitic grains may partially or totally transform into martensite. The goal is to determine the collective response of the aggregate of grains, where separate constitutive models are used for each phase. The main characteristics of the models are summarized in this section and the interested reader is referred to relevant publications for further details.

### 2.1. Elasto-plastic-transformation model for austenitic grains

The elastoplastic response of the austenitic phase and its possible transformation into martensite is simulated using the model originally developed by Turteltaub and Suiker [15–17] and subsequently extended by Tjahjanto et al. [34] and Yadegari et al. [35]. The model assumes that, upon loading, a region inside each grain (i.e. at the sub-grain length scale) may undergo a plastic deformation through slip and/or a sudden change in crystalline structure (i.e., a martensitic phase transformation). The transformation of austenite, which possesses a face-centered cubic (FCC) structure, into twinned martensite, composed of pairs of body-centered tetragonal (BCT) martensitic variants, is described according to

the theory of martensitic transformations [36]. The distinct pairs of (twinned) martensite, referred to as “transformation systems”, are characterized by two vectors, namely the habit plane normal and the shape strain vector. The transformation model is coupled to a crystal plasticity model to simulate sub-grain interactions in the austenite caused by transformation and plastic deformation [34]. Plastic deformation at the sub-grain level is described by slip occurring along active slip systems. Following the approach used in crystal plasticity, individual slip systems are characterized by a pair of vectors that represent the slip plane normal and the slip direction.

The sub-grain length scale behavior of a collection of slip systems and transformation systems is translated to the mesoscale (grain-level) by considering the weighted average of the active systems accounting for the corresponding inelastic mechanisms. This averaging procedure is performed within sub-regions in the grains, which allows for simulating non-homogeneous plastic deformations and/or transformations inside individual grains. The response contribution caused by the martensitic transformation is obtained upon time-integration of the rate of change of the volume fractions of the individual transformation systems. This set of rates is denoted as  $\dot{\xi} = (\dot{\xi}^{(1)}, \dots, \dot{\xi}^{(N)})$ , where  $\dot{\xi}^{(\alpha)}$  represents the rate of change of the volume fraction of the  $\alpha$ th martensitic system within a sub-region inside a grain and  $N$  is the total number of available transformation systems. The contribution of plasticity to the deformation is determined from the rate of slip in each system, i.e., from  $\dot{\gamma} = (\dot{\gamma}^{(1)}, \dots, \dot{\gamma}^{(M)})$ , where  $\dot{\gamma}^{(i)}$  denotes the rate of slip in the  $i$ th system and  $M$  is the total number of slip systems in the underlying material. Although the martensite is assumed to deform only elastically, the model takes into account the amount of plastic slip that occurred in the austenite prior to transformation.

The rates of change of transformation and plastic slip upon loading are modeled using a formulation that is thermodynamically-consistent with respect to the dissipation inequality. The isothermal model used in the present simulations is derived from a thermomechanical formulation using a constant homogeneous temperature such that the thermal deformation gradient is equal to identity [35]. Combining the formalism proposed by Onsager [37] with the so-called Coleman–Noll procedure [38], the terms in the dissipation inequality are expressed as a sum of products of affinities (i.e., driving forces) and fluxes (i.e., rates of change of martensitic volume fractions and plastic slip) for each inelastic mechanism. The model includes evolution equations between fluxes and affinities, known as the “kinetic relations”. In particular, the transformation of the austenitic phase into martensite is described by a tangent hyperbolic function that relates the rate of transformation of each individual transformation system to the driving force of the transformation system. Similarly, the plastic deformation in the austenite is governed by a power law that relates the plastic slip rate of each individual slip system to the corresponding plastic driving force. The evolution of plastic slip resistance is accounted for by a hardening power law. The kinetic relations are complemented by nucleation criteria describing the onset of inelastic deformation. Detailed expressions for the driving forces and the kinetic relations can be found in [15,17,34,35].

At the mesoscale (grain-level), the kinematical description of the austenitic phase is based on a large deformation framework where the deformation gradient at a given material point is multiplicatively decomposed as

$$\mathbf{F} = \mathbf{F}_e \mathbf{F}_p \mathbf{F}_{tr}, \quad (1)$$

with  $\mathbf{F}_{tr}$  is the transformation deformation gradient,  $\mathbf{F}_p$  the plastic deformation gradient and  $\mathbf{F}_e$  is the elastic deformation gradient. The mesoscale Cauchy stress tensor  $\mathbf{T}$  is determined from the elas-

tic deformation gradient and an effective stiffness for a mixture of austenite and martensite, see [17] for details. The mesoscopic Helmholtz energy, which contains contributions related to the “bulk” elastic strain energy, a surface energy and a lattice defect energy, is described by a state function that depends on the elastic Green–Lagrange strain defined as  $\mathbf{E}_e = (1/2)(\mathbf{F}_e^T \mathbf{F}_e - \mathbf{I})$  and on internal state variables. The internal state variables are the volume fractions of the transformation systems  $\xi$  and a so-called micro-strain  $\beta$  that is meant to reflect local elastic distortions in the crystalline lattice due to the presence of dislocations, see [34,35] for more details.

For evaluating the development of the martensitic transformation at the mesoscale, results are reported using the total martensitic volume fraction, defined as  $\xi_M = \sum_\alpha \xi^{(\alpha)}$ , with  $\xi_M = 1$  being reached for a fully-transformed sub-region inside an austenitic grain. In order to monitor the overall plastic deformation in the austenite, the accumulated amount of plastic slip is correlated to the elastic microstrain  $\beta_A$  in the austenitic phase, see [34] for more details.

## 2.2. Elastoplastic model for ferritic grains

The elastoplastic deformation of the ferritic grains is simulated using a crystal plasticity model suitable for the body-centered cubic (BCC) phase. The model is similar to the one used for the austenitic phase, except that it incorporates an additional term in the resistance to slip that accounts for non-symmetric behavior in the twinning and anti-twinning directions, see [39] for more details. At the mesoscale (grain-level), the kinematical description of the ferritic phase is decomposed as

$$\mathbf{F} = \mathbf{F}_e \mathbf{F}_p, \quad (2)$$

where the plastic deformation gradient  $\mathbf{F}_p$  is computed based on the contributions of the active slip systems. It is worth pointing out that the models used for the austenitic and ferritic phases are anisotropic, and explicitly incorporate the orientation of the underlying crystalline lattice.

## 3. Representative volume element

To establish a representative link between the mesoscale response, characterized by the individual behavior of the grains, and the macroscale response, governed by the collective behavior of a large number of grains, a material volume element containing a sufficiently large number of grains  $N_C$  must be analyzed, such that the average response of the aggregate does not vary as the number of grains is further increased, i.e., the macroscale response converges within a desired tolerance. A Representative Volume Element (RVE), comprising at least  $N_C$  grains, characterizes the converged macroscopic bulk response of the material. Note that the establishment of an RVE depends on the choice of the quantities used to monitor convergence. Since the current study aims at establishing the macroscopic mechanical response, the major components of the stress are chosen as the primary quantities of interest for the establishment of an RVE. In a multiscale framework, the upper scale does not contain an explicit constitutive relation; instead, the response relies on information obtained from the lower scale that is necessary to provide a macroscopic state of equilibrium under quasi-static loading conditions. In other words, the average stress is directly computed from lower scale information. In order to establish an RVE based on convergence of other quantities, such as the crystallographic texture or the internal variables, typically a different number of grains is required than when using the macroscopic stress parameters.

### 3.1. Microstructural volume elements

For identifying the minimum number of grains required for establishing an RVE, the responses of seven microstructural samples are analyzed. The samples consist of aggregates of ferritic and austenitic grains with the total number of grains increasing from 8 to 800, as indicated in Table 1. The volume fraction of the secondary phase (austenite) in each sample is approximately 12%, which is a common value for multiphase TRIP steels, see, e.g., [1,3]. The geometrical construction of the microstructures is achieved with a newly-developed algorithm that is based on the generation of Voronoi-shaped polyhedrons. A typical result of this approach is illustrated in Table 2, representing the three-dimensional samples used in the morphology study presented in Section 4. The dispersed microstructures depicted in the first row of Table 2 have comparable grain structures as the samples used in the current convergence analysis, where it can be observed that some of the grains have non-convex shapes. Standard Voronoi cells, however, are convex, which limits their capacity to mimic realistic metallic microstructures with arbitrary (convex and non-convex) grain shapes. The specific geometries of these grains result from complex grain growth and grain shrinkage interactions activated during the thermal processing of a multiphase steel [40]. In order to account for non-convex grains in the numerical simulation of a steel’s microstructure, a new algorithm, based on the generation of a *multilevel Voronoi tessellation*, has been developed. Accordingly, at the first level a standard periodic Voronoi tessellation is generated, i.e., seed points are chosen randomly within a cubic region, and this local seed point field is fully replicated in 26 adjacent cubic regions, which together form a regular  $3 \times 3 \times 3$  stacking of cubes. As a next step, Voronoi cells are generated from the complete, periodic seed point field in the stacking of 27 cubic domains. The structure of the Voronoi cells is periodic over each of the 27 cubes, where the cells intersecting with the 6 outer faces of the stacking of cubes are cut to fit exactly within the overall domain. These first-level Voronoi cells are referred to as the *fine* tessellation. At the second level, a *coarser* tessellation is created, also with a randomly-chosen seed point field, but with a smaller seed point density compared to the density of the first tessellation. Cells from the coarse tessellation are used as master regions for the construction of complex-shaped grains. To this end, all cells of the finer tessellation, whose seed points are located in the interior of the same master cell, are merged to form a single grain. This procedure is illustrated in Fig. 1 for the two-dimensional case. By modifying the point field densities at both levels (fine and coarse), it is possible to generate a broad range of different shapes and sizes of grains. With this approach, a good resemblance with complex, realistic metallic microstructures may be obtained.

The next step is to assign a specific phase to each grain constructed. In the present study, two phases are distributed within the microstructure, namely ferrite and austenite, where their volume fractions are defined a priori. For the samples indicated in Table 1, the spatial distribution of the secondary phase (austenite) inside the matrix (ferrite) is performed randomly. An iterative

**Table 1**

Composition and volume fraction of different microstructural samples used in the RVE convergence study.

Sample #	Austenitic grains	Ferritic grains	Volume fraction
1	1	7	12.0
2	8	56	12.1
3	12	88	12.2
4	24	176	11.9
5	56	394	12.0
6	72	525	12.0
7	100	700	11.9

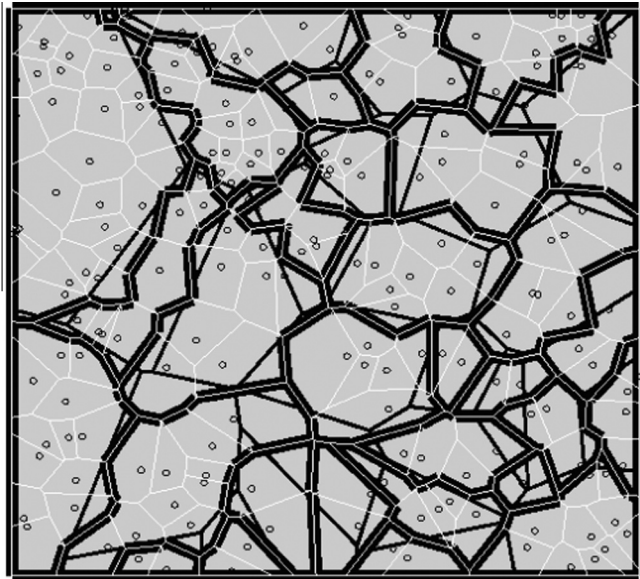


**Fig. 1.** Two-dimensional illustration of a microstructure obtained from a multilevel Voronoi tessellation. The first level (fine tessellation) contains 200 cells and the second level (coarse tessellation) is characterized by 30 cells. The thin white lines and small circles show, respectively, the cells and Voronoi seed points of the first-level tessellation. The thin black lines show the cells of the second-level tessellation. The bold black lines illustrate the resulting complex-shaped grain structure. The grain size is largely determined by the coarse tessellation while the fine tessellation controls the grain morphology, particularly the grain boundaries.

procedure is employed for approaching the specified volume fractions of the phases (i.e., 12% austenite, 88% ferrite) within a small tolerance. Subsequently, a finite element model is constructed for simulating the material behavior of this microstructure, where the specific phase and crystal orientation for each finite element are assigned in accordance with the location of the element centroid in the underlying multilevel Voronoi tessellation. Since the structure of the finite element mesh generally does not exactly follow the orientations of the grain boundaries in the multilevel Voronoi tessellation, some discrepancies are introduced in the local stress and deformation fields near grain boundaries. However, these discrepancies automatically diminish under mesh refinement, and therefore generate a negligible effect on the accuracy of the simulation result if the finite element mesh is chosen sufficiently fine. Specific details of a mesh refinement study are presented in Section 3.3. Furthermore, since local grain boundary effects, such as dislocation pile-up, intergranular fracture, and void nucleation, are not considered in the present study, the exact modeling of the grain boundary geometry may be presumed to be of lower relevance.

### 3.2. Crystallographic orientation

In the present study the orientation distribution of an aggregate of grains is assumed to be *isotropic* for both the austenitic and ferritic phases. The orientation of the crystalline lattice of an individual grain with respect to a global vector basis is described in terms of three Euler angles, by applying the 313 rotation sequence about the three corresponding axes of rotation. In order to cover the whole orientation space without using the symmetry properties of the underlying crystalline structure, the three Euler angles range, respectively, from 0 to  $2\pi$ , 0 to  $\pi$  and 0 to  $2\pi$ . For a sufficiently large number of grains, a uniform (isotropic) orientation distribution can be achieved by choosing the three Euler angles as, respectively,  $2\pi a$ ,  $\cos^{-1}(2b-1)$ , and  $2\pi c$ , where  $a$ ,  $b$  and  $c$  are random variables ranging between 0 and 1. Note that the

expression used for the second Euler angle guarantees an unbiased orientation distribution by decoupling the composite Euler rotations. For each of the samples indicated in Table 1, four distinct random orientation distributions are chosen to study the influence of the grain orientation. Typical distributions, displayed as [100]-pole figures, are shown in Fig. 2 for the first, fourth and seventh sample listed in Table 1.

### 3.3. Numerical simulations

All samples are subjected to an *average* simple shear deformation  $\bar{\mathbf{F}} = \mathbf{I} + \bar{\gamma} \mathbf{e}_1 \otimes \mathbf{e}_3$  where  $\bar{\gamma}$  is the amount of shear,  $\mathbf{e}_i$  with  $i = 1, 2, 3$  is an orthonormal basis aligned with the cubic samples, and  $\otimes$  denotes the tensor product. The samples are quasi-statically loaded up to  $\bar{\gamma} = 0.2$  with an applied rate of deformation equal to  $10^{-4} \text{ s}^{-1}$ . Simple shear is chosen as the governing deformation mode here, because previous simulations performed on single crystals of austenite indicated that the activation of transformation by shear, somewhat counter intuitively, leads to the development of substantial normal stresses, see [17]. In the present study this transformation mechanism is examined in detail for different microstructures, thereby illustrating its effect on the untransformed austenite and the ferritic matrix in terms of the generated plastic deformation, i.e., the TRIP-effect. In addition, damage effects not included in the present model, such as void nucleation and intergranular fracture, are less sensitive to simple shear than to other elementary types of loading, such as uniaxial tension or hydrostatic tension. For simplicity reasons, it is thus allowed to ignore these effects in the present study, and essentially focus upon the interplay between transformation and plasticity. Details on the extension of the phase transformation model with the effect of anisotropic crystalline damage, however, can be found in [41,42].

On the outer surfaces of the cubic sample the boundary conditions are modeled as periodic, which ensures that the average deformation gradient corresponds to the prescribed value  $\bar{\mathbf{F}}$  during loading, i.e.,  $\langle \mathbf{F} \rangle = \bar{\mathbf{F}}$ , where  $\langle \cdot \rangle$  denotes the volume average. The details of the numerical implementation of a *non-redundant set of periodic boundary conditions* are presented in A. It is worth mentioning that simulations carried out with periodic boundary conditions generally provide a softer response – and usually a physically more meaningful prediction – compared to simulations based on pointwise affine boundary conditions. All simulations are performed with a regular finite element mesh of  $30 \times 30 \times 30$  (=27,000) elements, using linearcubical elements with reduced integration. A mesh refinement analysis (not presented here) has indicated that this mesh density is sufficiently fine for capturing the effective response of the sample in an accurate fashion; for an arbitrarily chosen microstructure a further refinement towards a regular mesh of  $40 \times 40 \times 40$  (=64,000) elements increased the accuracy of the effective (shear) stress response by at most 2%, and further did not have a qualitative effect on the results found for four distinct random orientation distributions.

In the simulations, the computation of the Cauchy stress, stiffness and internal variables in individual material points is performed incrementally in time by using an implicit iterative update scheme formulated within a large deformation framework. The details of this numerical implementation can be found in [16]. A complete list of the material parameters adopted in the constitutive models for the different phases can be found in Table 1 of reference [35]. This list shows that the martensite is modeled as the stiffest phase, followed by the austenite and, slightly below, the ferritic phase. For the austenite the ultimate slip resistance used in the crystal plasticity model equals 579 MPa, which is about 1.4 times the value adopted for the softer ferritic phase (412 MPa). As mentioned previously, the martensite in TRIP steels

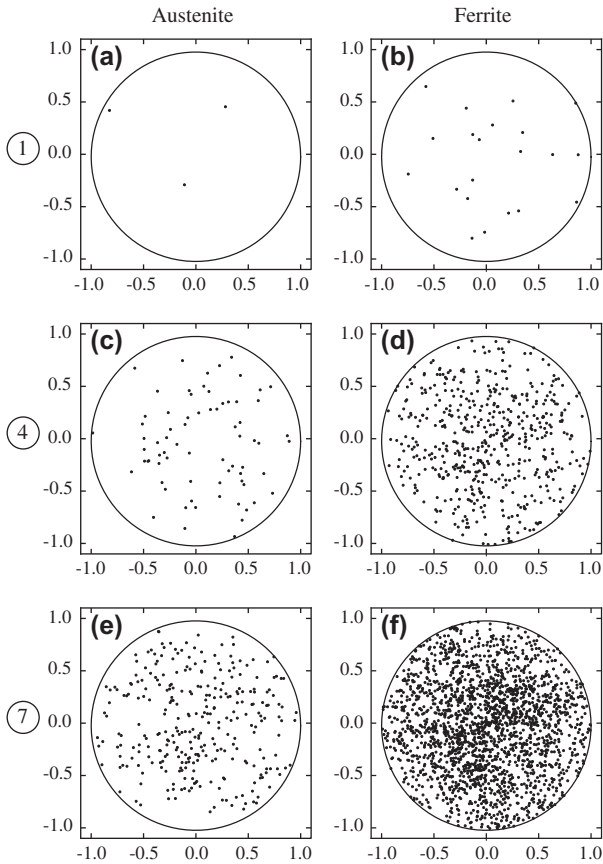


**Fig. 2.** Typical [100]-pole figures indicating the orientation distributions of the first sample (a and b), fourth sample (c and d) and seventh sample (f and g) listed in Table 1. The left column corresponds to austenite and the right one to ferrite.

is relatively hard, and therefore may be assumed to deform purely elastically.

The results of a typical set of simulations for four distinct, randomly-chosen crystal orientation distributions (indicated as O1, O2, O3 and O4) that are successively used in the same volume element (in this case sample 4 listed in Table 1) are shown in Fig. 3 as a function of the average amount of shear  $\bar{\gamma}$ . Fig. 3(a) and (b) indicates the average Cauchy stress components  $\bar{T}_{31}$  and  $\bar{T}_{11}$ , respectively, with the average determined over all grains (ferrite and austenite). Fig. 3(c) shows the average microstrain in the ferrite (averaged over ferritic grains only) and Fig. 3(d) shows the average total volume fraction of martensite  $\bar{\xi}_M$  (averaged over austenitic grains only). For sample 4, the influence of the crystal orientation distribution on the plastic response of the ferritic matrix, which is monitored using the average microstrain  $\bar{\beta}_F$ , is relatively small as shown in Fig. 3(c). However, the crystal orientation has a relatively important effect on the response of the austenitic grains (secondary phase) as may be inferred from Fig. 3(d), showing the evolution of the average normalized martensitic volume fraction  $\bar{\xi}_M$ . Since sample 4 contains 176 grains of ferrite but only 24 grains of austenite, it is expected that the scatter of the responses of the secondary phase is larger than for the primary phase. Due to the distinct evolutions of the martensitic phase transformation in the secondary phase for different crystal orientation distributions, the average Cauchy stress component  $\bar{T}_{11}$  also evolves quantitatively differently as may be observed from Fig. 3(b). Similar results (not shown here) were obtained for the average stress components  $\bar{T}_{22}$  and  $\bar{T}_{33}$ . Nevertheless, the influence of the crystal orientation is less noticeable for the main average Cauchy shear stress component  $\bar{T}_{31}$ , as can be seen in Fig. 3(a). This trend can be ascribed to

the fact that a phase transformation induces a (local) volumetric expansion, which needs to be compensated for by a volumetric contraction elsewhere in the domain, i.e., in the untransformed austenite and/or the ferritic matrix. This is, since the imposed average simple shear deformation is isochoric. Because the normal components are affected by the (average) bulk properties, this dilatation has a stronger effect on the average normal stresses  $\bar{T}_{ii}$ ,  $i = 1, 2, 3$ , than on the average shear stress  $\bar{T}_{31}$ . The dilatation of the secondary phase is thus responsible for both the negative values for the average normal stresses, as well as for a larger scatter in their responses compared to the average shear stress. In particular, observe that the normal (compressive) stress  $\bar{T}_{11}$  for orientation O1 is the largest (in absolute value) of all orientations analyzed, which correlates with the highest amount of transformation  $\bar{\xi}_M$  obtained for the same orientation. The influence of the crystal orientation on the response of the computational samples is analyzed further in the next section.

### 3.4. Convergence analysis

In order to establish a lower bound for the number of grains required for an RVE, the final states of the simulations (i.e., at  $\bar{\gamma} = 0.2$ ) for the seven volume elements indicated in Table 1 are plotted in

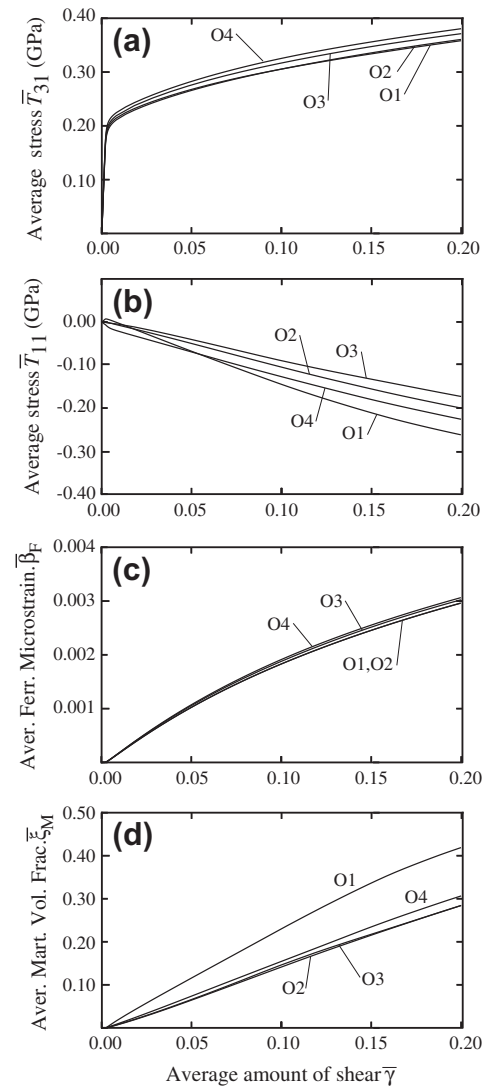


**Fig. 3.** Typical results of simulations for sample 4 (which contains a total of 200 grains, see Table 1) for four distinct crystal orientations, labeled O*i*, with  $i = 1, \dots, 4$ .

Fig. 4. This is done in terms of average Cauchy stress components and in Fig. 5 in terms of the average plastic deformation (which directly relates to the average microstrain  $\beta$ , see [34]) in the ferritic and austenitic grains and the average volume fraction of martensite. In Figs. 4 and 5 the results are shown as a function of the total number of grains in the samples (which are also labeled with the corresponding sample numbers indicated in Table 1). For each sample, the four data points, shown as crosses, correspond to the results of four distinct random crystal orientations. To better visualize these results, an interpolated area bounded by the upper and lower simulation values is shaded in gray and the interpolated mean value of the four orientation distributions is shown by a dotted line.

From Fig. 4(a), it can be observed that the main shear stress component  $\bar{T}_{31}$  converges, within an acceptable tolerance, for samples comprising about 200 grains or more. The plastic deformation in the ferritic matrix also converges for a similar number of grains, as can be seen in Fig. 5(a) in terms of the microstrain  $\bar{\beta}_F$ . However, the convergence of the normal stress components  $\bar{T}_{ii}$ ,  $i = 1, 2, 3$ , is relatively low as shown in Fig. 4. The low rate of convergence on

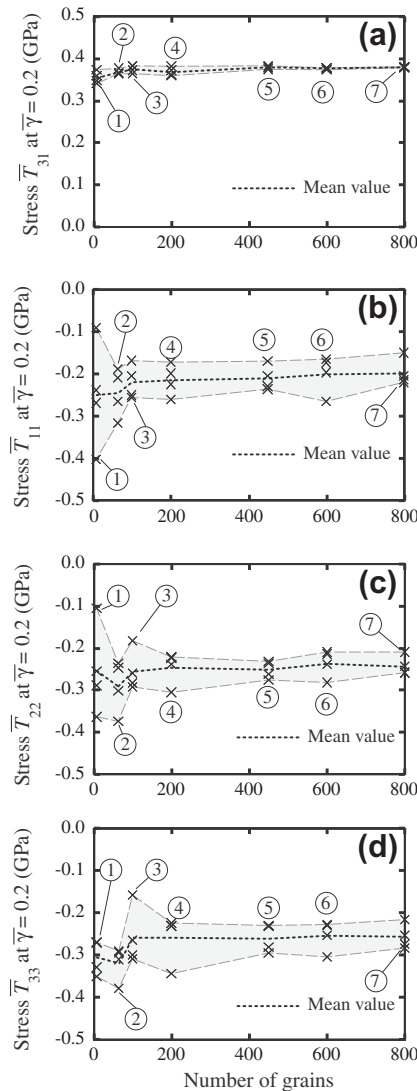


Fig. 4. Average stress state of volume elements at  $\bar{\gamma} = 0.2$ : (a)–(d) Cauchy stress components  $\bar{T}_{31}$ ,  $\bar{T}_{11}$ ,  $\bar{T}_{22}$  and  $\bar{T}_{33}$ , respectively. The crosses represent the values found for the four distinct random crystal orientations. The dashed lines connect the upper and lower values and bound the interpolated area shaded in gray. The dotted line reflects the interpolated mean value. The numbers designate the samples listed in Table 1.

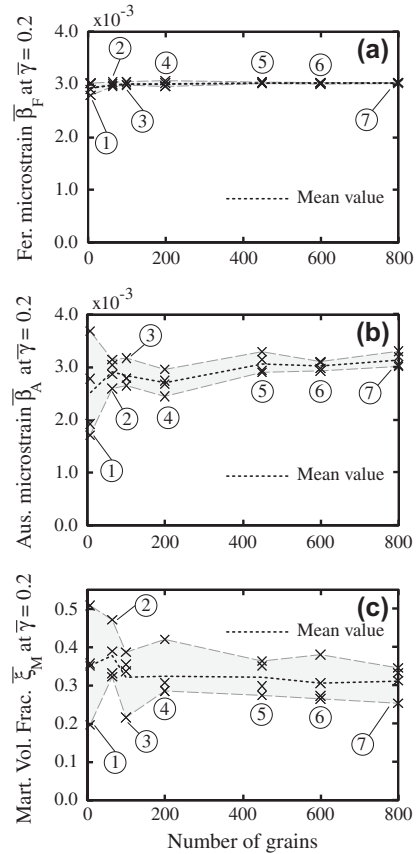


Fig. 5. Average state variables of volume elements at  $\bar{\gamma} = 0.2$ : (a) ferritic microstrain  $\bar{\beta}_F$ , (b) austenitic microstrain  $\bar{\beta}_A$  and (c) normalized martensitic volume fraction  $\bar{\epsilon}_M$ . The crosses represent the values found for the four distinct random crystal orientations. The dashed lines connect the upper and lower values and bound the interpolated area shaded in gray. The dotted line reflects the interpolated mean value. The numbers designate the samples listed in Table 1.

the normal stress components can be traced back to the low rate of convergence of the response of the secondary phase, austenite, as discussed in Section 3.3. Indeed, as can be inferred from Fig. 5(b) and (c), the inelastic response of the secondary phase, measured in terms of the amount of plastic deformation in the austenite and its transformation into martensite, shows a scatter due to the limited number of austenitic grains in the samples, see Table 1. Nevertheless, as may be observed in Figs. 4 and 5, three out of the four simulations for the largest sample (sample 7, with 100 grains of austenite) already show a reasonable convergence as these results are clustered closely around the mean value.

The convergence analysis indicates that the macroscopic shear stress in a multiphase steel under simple shear may be determined with a relatively small number of total grains (e.g., 200 grains, in accordance with sample 4 listed in Table 1), but the macroscopic normal stress components require a larger number of grains of the secondary phase. Reasonable results may be expected with about 100 grains of the secondary phase and 800 grains in total, i.e., sample 7 listed in Table 1. These guidelines are used in the next section to study the effect of the spatial distribution of the secondary phase on the overall response of a multiphase steel.

#### 4. Effect of a banded microstructure on the response of a multiphase steel

The influence of the spatial distribution of the secondary phase (austenite) on the macroscopic properties of a multiphase steel is analyzed. For this purpose, the mechanical behavior of a

material where the austenitic grains are clustered in a plate-like region (band) is compared with the response of a benchmark microstructure where the austenitic grains are randomly scattered within the ferritic matrix. These two microstructures are henceforth referred to as the *banded* and the *dispersed* microstructures, respectively.

4.1. Volume elements with banded microstructure

The analysis is carried out for three pairs of banded and dispersed microstructures with austenitic volume fractions of 10%, 20% and 30%, as shown in Table 2. The microstructural samples were generated using the same multi-level periodic Voronoi tessellation as described in Section 3. The banded microstructures were created by defining a banded region and, within that region, assigning grains to the austenitic phase iteratively until the overall volume fraction of austenite approximately matched the target value prescribed a priori. As indicated in Table 2, all microstructures contain more than 200 grains in total, which was identified in Section 3.4 as the threshold for an RVE deduced from the macroscopic shear stress. The microstructures contain between 47 and 144 grains of the secondary phase (austenite), which should provide reasonable to accurate predictions for the normal stresses and the internal variables. As a result of the application of a multilevel Voronoi tessellation, there are less grains of austenite in the banded microstructures than in the dispersed microstructures. Hence, nominally the austenitic grains in the banded microstructures are larger than those in the dispersed microstructures. The difference in average austenitic grain size of the banded and dispersed microstructures ranges from 13% to 22%, which is relatively small. Moreover, since the purpose of the present analysis is to study the effect of the spatial distribution of the austenite rather than to study grain size effects, a length scale parameter in the model that is related to the grain size (see [27] for more details) was kept the same for all simulations.

4.2. Numerical simulations with banded microstructures

As in Section 3, all microstructures considered are subjected to a macroscopic simple shear of  $\bar{\gamma} = 0.2$ . The loading rate and periodic boundary conditions are the same as those of the simulations discussed in Section 3.3. Randomly-chosen crystal orientations, as explained in Section 3.2, are used in the simulations. Although some fluctuations in the response may still occur for distinct randomly-chosen crystal orientations, based on the number of grains used in the samples, see Table 2, it is expected from the convergence study in Section 3.4 that these do not strongly affect the result.

As opposed to a dispersed microstructure, which is essentially macroscopically isotropic, a banded microstructure may be sheared in distinct ways depending on the orientation of the shearing direction and shearing plane with respect to the band-like region in which the secondary phase is clustered. This motivates separate simulations and comparisons of the samples for different shear loading cases. Two extreme shear loading cases are shown in Fig. 6, where the plate-like austenitic region is represented as an

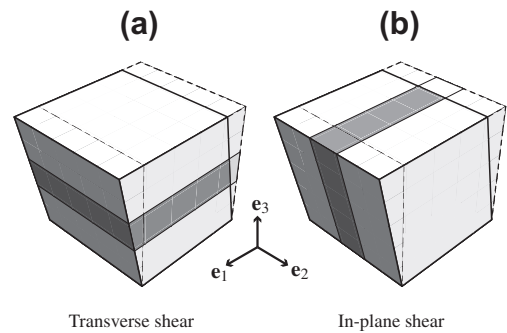
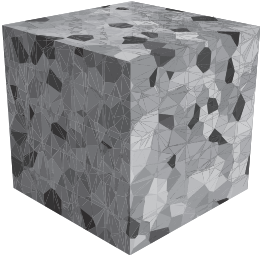
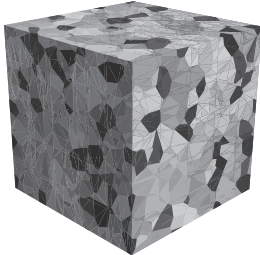
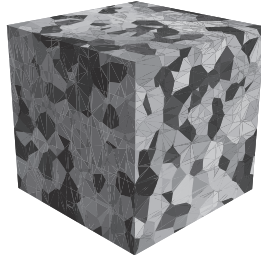
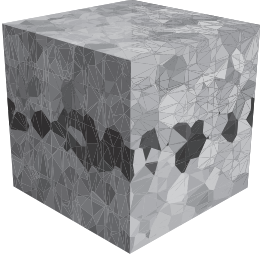
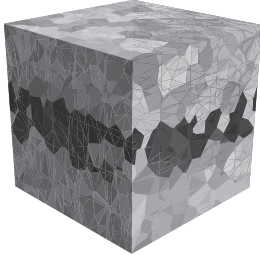
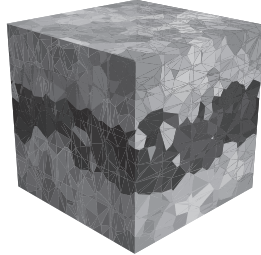


Fig. 6. Simple shear naming convention with respect to the band's plane: (a) transverse shearing case and (b) in-plane shearing case. The dark gray band represents the region where the austenitic grains are clustered.

Table 2

Microstructures constructed from a multilevel Voronoi tessellation, using three distinct initial volume fractions of austenite of 10%, 20% and 30%. Austenitic grains are displayed in dark gray while ferritic grains are shown in light gray. The microstructures with randomly-dispersed austenitic grains are shown in the top row while the banded microstructures are indicated in the bottom row. The number of austenitic and ferritic grains is indicated below each sample.

10% Volume fraction	20% Volume fraction	30% Volume fraction
		
Austenite: 77 Ferrite: 194	Austenite: 122 Ferrite: 193	Austenite: 144 Ferrite: 187
		
Austenite: 47 Ferrite: 197	Austenite: 67 Ferrite: 178	Austenite: 99 Ferrite: 160



idealized band in the middle of a cubic-sample. The two loading cases are referred to as *transverse* and *in-plane* shearing, respectively. Other possible shearing directions have been omitted for brevity because their responses are bounded by the results of the in-plane and transverse shear loading cases.

The average Cauchy shear stress component  $\bar{T}_{31}$ , the average normalized martensitic volume fraction  $\bar{\xi}_M$  and the average ferritic microstrain  $\bar{\beta}_F$  are shown as functions of the average amount of shear  $\bar{\gamma}$  in Fig. 7 for the transverse shear loading case and in Fig. 8 for the in-plane shear loading case. The results for the banded microstructures are indicated by the black curves and for the benchmark dispersed microstructures by the gray curves. Dotted, dashed and solid lines are used to represent the results for microstructures with, respectively, 10%, 20% and 30% volume fraction of austenite.

#### 4.3. Influence of the initial austenitic volume fraction

From Fig. 7(a), which corresponds to the transverse shear loading case, it can be observed that for the microstructures with

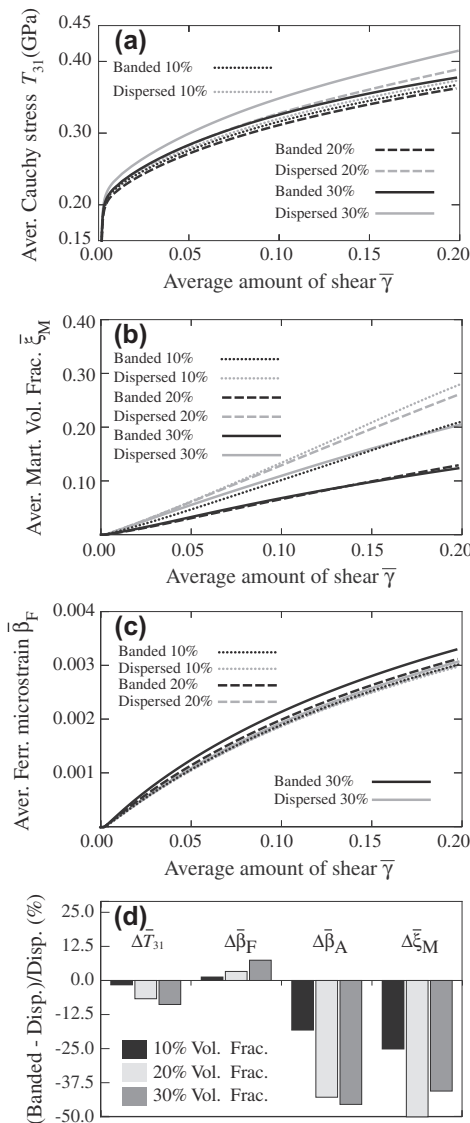


**Fig. 7.** Evolution under transverse shear loading of (a) the average main Cauchy shear stress, (b) the average martensitic volume fraction and (c) the average ferritic microstrain as functions of the macroscopic amount of shear. Graph (d) contains the relative difference between the response at  $\bar{\gamma} = 0.2$  of the banded and dispersed microstructures.

dispersed grains of austenite (gray lines) the shear strength increases with increasing initial volume fraction of austenite. However, for the banded microstructures (black lines), the trend is not monotonic as the response of the sample with 10% austenite has a slightly higher strength than the sample with 20% austenite. Essentially, an increase of the shear strength by a higher initial volume fraction of austenite in the banded microstructure only becomes noticeable when further increasing the initial volume fraction to 30% austenite. In contrast, under in-plane shearing the dependence of the shear strength on the austenitic volume fraction is similar for the dispersed and banded microstructures, see Fig. 8(a). In this case the shear strength always increases with an increasing initial volume fraction of austenite.

Although strictly speaking there is no monotonic dependence of the martensitic transformation rate on the initial volume fraction of austenite, from Figs. 7(b) and 8(b) it may be concluded that the general trend is that the martensitic transformation rate under simple shear *decreases* with increasing austenitic volume fraction. This trend applies to both the transverse and in-plane shear loading cases. Note, however, that this trend refers to the amount of martensite formed in the austenitic grains and not to the total amount of martensite in the sample, which depends on the initial volume fraction of austenite. Indeed, despite that the transformation rate becomes smaller with increasing initial volume fraction of austenite, the *total* amount of martensite formed during deformation *increases* with an increasing initial volume of austenite. Because the martensite is a relatively hard phase, this effect increases the effective shear strength of the sample, see Figs. 7(a) and 8(a).

The plastic deformation in the ferrite appears to be rather insensitive to the initial volume fraction of austenite, except for the banded microstructure under transverse shear loading, where the plastic deformation in the ferrite slightly increases with increasing initial volume fraction of austenite, see Fig. 7(c).

#### 4.4. Influence of the spatial distribution of austenite

In order to compare the responses of the banded and dispersed microstructures for samples with an equal amount of austenite, the relative differences between the shear stress, martensitic volume fraction and microstrains of the banded and dispersed microstructures at the end of the simulations are graphically summarized in Figs. 7(d) and 8(d) for the transverse and in-plane shear loading cases, respectively. The relative difference for the effective shear stress is defined as

$$\Delta\bar{T}_{31} = \frac{\bar{T}_{31}^{\text{banded}} - \bar{T}_{31}^{\text{dispersed}}}{\bar{T}_{31}^{\text{dispersed}}}\bigg|_{\bar{\gamma}=0.2},$$

and similar formulas are used for the internal variables.

It can be observed from Fig. 7(d) that for all austenitic volume fractions analyzed the banded microstructures have a lower shear strength than the dispersed ones under transverse shear, i.e., the values of  $\Delta\bar{T}_{31}$  are negative. Moreover, the absolute value of the relative difference in shear strength, as indicated by  $|\Delta\bar{T}_{31}|$ , increases with an increasing initial volume fraction of austenite. This trend may be correlated to the response of the secondary phase (austenite) and its effect on the primary phase (ferrite). Indeed, as illustrated in Fig. 7(d), the amount of transformation as well as the plastic deformation in the austenite are significantly lower in the banded microstructures than in the dispersed microstructures (up to 50% difference). Observe that within the austenitic phase a decrease in transformation is not compensated for by an increase in plastic deformation. Rather, both inelastic mechanisms within the austenite show the same decreasing trend, i.e., less plastic deformation and less transformation for the banded microstructure compared with the dispersed microstructure. This indicates

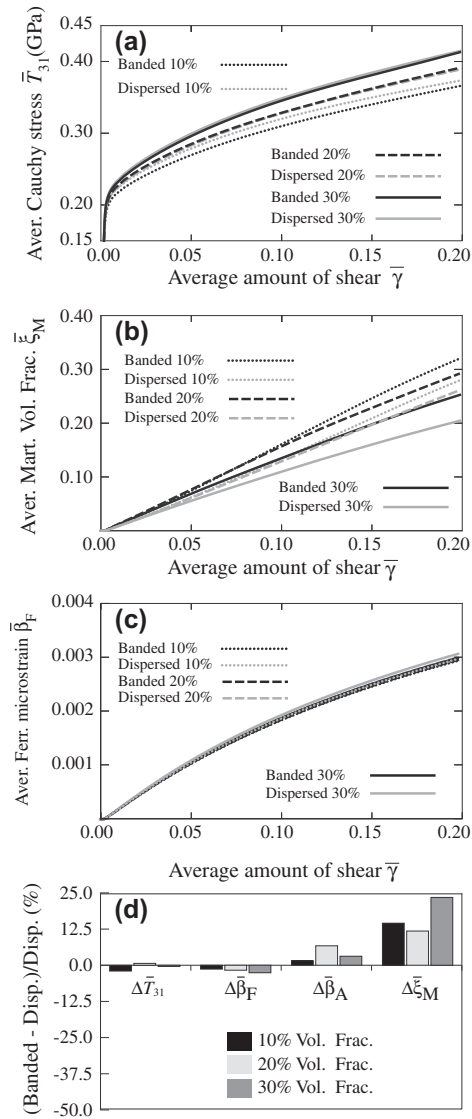


**Fig. 8.** Evolution under in-plane shear loading of (a) the average main Cauchy shear stress, (b) the average martensitic volume fraction and (c) the average ferritic microstrain as functions of the macroscopic amount of shear. Graph (d) contains the relative difference between the response at  $\bar{\gamma} = 0.2$  of the banded and dispersed microstructures.

that the austenite tends to deform less when it is clustered around a band-like region compared with microstructures with randomly distributed grains of austenite inside the ferritic matrix. Correspondingly, in order to achieve the same imposed average shear deformation, the ferritic matrix tends to deform more for the banded microstructures than for the dispersed microstructures. This behavior can be confirmed from the values of  $\Delta\bar{\beta}_F$ , which measures the differences between the microstrains in the ferritic matrix of the banded and dispersed microstructures, as shown in Fig. 7(d). Indeed, the amount of plastic deformation in the ferritic matrix is higher for banded microstructures than for dispersed ones, which in relative terms diminishes the contribution to the overall strength of the (harder) secondary phase in banded microstructures. This prediction of the simulations is consistent with experimental observations reported in [29], albeit for tensile tests. In the experiments a significant portion of the deformation was carried by the ferritic matrix while the austenite in the banded regions experienced a smaller deformation and, consequently, a rel-

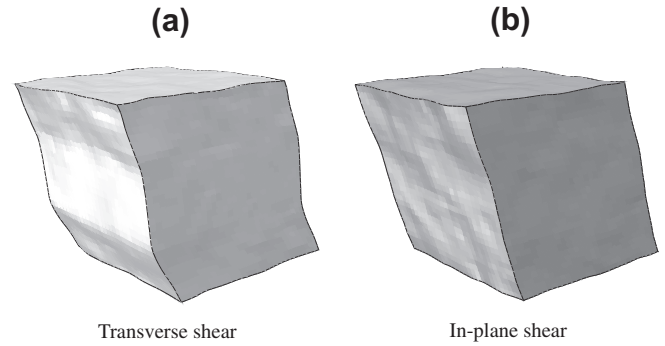


**Fig. 9.** Deformed shape at  $\bar{\gamma} = 0.2$  of banded microstructure for (a) transverse shear and (b) in-plane shear for samples with 30% initial volume fraction of austenite.

atively small transformation rate. The authors attributed the reduction in transformation rate to unfavorable crystal orientations with respect to the external loading; however, the present simulations suggest that a low transformation rate in the austenitic band-like region may be ascribed to a relatively high plastic deformation of the ferritic matrix.

For the in-plane shear loading case, the shear strength of the banded microstructures is somewhat similar to the strength of the corresponding dispersed microstructures, as can be observed from Fig. 8(a) and 8(d). In contrast to the transverse shear loading case, under in-plane shear loading there is *more* transformation and plastic deformation in the austenite for the banded microstructures than for the dispersed microstructures, see Fig. 8(b) and (d). Correspondingly, there is *less* plastic deformation in the ferrite for banded microstructures than for dispersed microstructures, see Fig. 8(c) and (d). Nevertheless, the distinct behavior of the banded and dispersed microstructures under in-plane shear is not sufficient to reach significantly different shear strengths.

In order to gain a better insight in the different responses of banded microstructures under transverse and in-plane shearing, the deformed shapes of the samples are shown in Fig. 9 (see also the sketch in Fig. 6). The samples depicted in the figure correspond to 30% initial volume fraction of austenite. As illustrated in Fig. 9(a), the austenitic region deforms less than the ferritic matrix under transverse shear loading. In this case the softer ferritic matrix carries most of the deformation. In contrast, the deformation under in-plane shear loading is more homogeneous, hence the shear deformation is more evenly distributed between the ferrite and austenite. Correspondingly, the austenitic region carries a relatively smaller amount of the load under transverse shear than under in-plane shear. Indeed, the average shear stress in the austenite,  $\bar{T}_{31}^A$ , at the end of the simulation is 400 MPa for the transverse shear loading case and 537 MPa for the in-plane shear loading case. The corresponding average shear stresses in the ferrite,  $\bar{T}_{31}^F$ , are 367 MPa for the transverse shear loading case and 359 MPa for the in-plane shear loading case. Since for both loading cases the average stresses in the ferrite are similar, the shear stress  $\bar{T}_{31}$  averaged over the whole domain is lower under transverse loading (377 MPa) than under in-plane loading (413 MPa).

## 5. Conclusions

A convergence analysis was carried out to establish the size of representative volume elements for multiscale simulations using non-convex grain shapes that are generated from a multilevel Voronoi tessellation. From the numerical simulations of microstructures with banded and dispersed austenitic grains, it was found that:

- The shear strength of a TRIP steel increases with increasing volume fraction of austenite for microstructures with grains of austenite being randomly dispersed within a ferritic matrix. For microstructures with clustered austenitic grains in band-like regions, the shear strength does not necessarily increase with an increasing volume fraction of austenite.
- For a TRIP steel sample that contains a banded microstructure and is loaded under transverse shear the plastic deformation localizes in the softer ferritic matrix, which diminishes the strength contribution of the secondary austenitic phase.
- The shear strength of a TRIP steel with clustered grains of austenite in a band-like region may be lower than the shear strength of a steel with a similar composition but with the austenitic grains being dispersed in the ferritic matrix.

From the above findings it may be concluded that clustering of the austenite in band-like regions in general has a negative effect on its contribution to the effective hardening of the sample.

### Acknowledgments

This research is supported by the Technology Foundation STW, applied science division of the Organization for Scientific Research (NWO) and the Technology Program of the Ministry of Economic Affairs of the Netherlands through STW-MuST (Multiscale Simulation Techniques) Project 10117.

### Appendix A. Non-redundant periodic boundary conditions

In order to have a consistent transition between two different scales, the volume average of the deformation gradient in a given microstructural volume element should be equal to the prescribed deformation gradient  $\bar{\mathbf{F}}$  from the upper scale, i.e.,

$$\langle \mathbf{F} \rangle := \frac{1}{|\Omega|} \int_{\Omega} \mathbf{F} dV = \bar{\mathbf{F}}, \quad (\text{A.1})$$

where  $|\Omega|$  denotes the volume of the microstructural domain. Since  $\bar{\mathbf{F}}$  is constant over the domain, (A.1) can be written as

$$\int_{\Omega} \nabla(\mathbf{u} - (\bar{\mathbf{F}} - \mathbf{I})\mathbf{x}) dV = \mathbf{0}, \quad (\text{A.2})$$

with  $\mathbf{u}$  being the displacement field,  $\mathbf{I}$  the identity tensor and  $\mathbf{x}$  a material point in the reference configuration. A straightforward application of the divergence theorem results in the following expression:

$$\int_{\partial\Omega} \mathbf{n} \otimes (\mathbf{u} - (\bar{\mathbf{F}} - \mathbf{I})\mathbf{x}) ds = \mathbf{0}, \quad (\text{A.3})$$

where  $\partial\Omega$  is the external surface of the domain and  $\mathbf{n}$  is the outward unit normal vector. Henceforth, it is assumed that the microstructural domain  $\Omega$  is a cube of edge length  $h$  and the edges are aligned with a global basis  $\mathbf{e}_i$ ,  $i = 1, 2, 3$ , as shown in Fig. A.10. Sufficient conditions for (A.1) to hold can be inferred from (A.3) in terms of the relative displacements of parallel faces of the cube, i.e.,

$$\begin{aligned} \mathbf{u}_{F1} - \mathbf{u}_{F2} &= \mathbf{a}_1 := (\bar{\mathbf{F}} - \mathbf{I})h\mathbf{e}_1, \\ \mathbf{u}_{F3} - \mathbf{u}_{F4} &= \mathbf{a}_2 := (\bar{\mathbf{F}} - \mathbf{I})h\mathbf{e}_2, \\ \mathbf{u}_{F5} - \mathbf{u}_{F6} &= \mathbf{a}_3 := (\bar{\mathbf{F}} - \mathbf{I})h\mathbf{e}_3, \end{aligned} \quad (\text{A.4})$$

where  $\mathbf{u}_{Fi}$ , with  $i = 1, \dots, 6$ , denote the surface displacement for points on the  $i$ th surface of the cube, see Fig. A.10. The vectors  $\mathbf{a}_1, \mathbf{a}_2$  and  $\mathbf{a}_3$ , defined in (A.4), are assumed to be known. While Eqs. (A.4) are sufficient for satisfying the periodicity condition on the external boundary of the domain, this system of equations contains redundant information for points on the external corners and

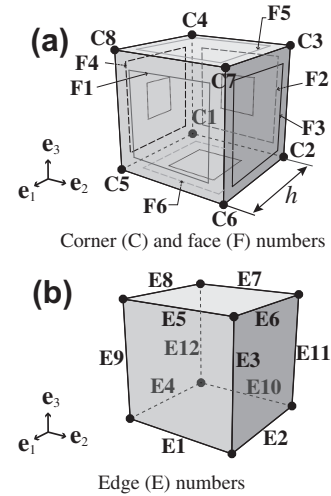


Fig. A.10. Labeling convention for (a) external faces and corners and (b) edges of the computational domain.

edges of the cube, which may potentially cause problems in numerical implementations. To avoid this redundancy, one has to establish the minimum number of independent relations (corner-to-corner and edge-to-edge relations) that preserve periodicity.

For the corner points, there are 12 relations that can be obtained from (A.4), namely

$$\begin{aligned} \mathbf{u}_{C5} - \mathbf{u}_{C1} &= \mathbf{a}_1, \\ \mathbf{u}_{C6} - \mathbf{u}_{C5} &= \mathbf{a}_2, \\ \mathbf{u}_{C7} - \mathbf{u}_{C6} &= \mathbf{a}_3, \\ &\vdots \end{aligned} \quad (\text{A.5})$$

with other relations between corner points obtained in a similar fashion. In (A.5),  $\mathbf{u}_{Ci}$ , with  $i = 1, \dots, 8$ , denotes the displacement of the  $i$ th corner point. This system of equations has a rank deficiency of five (only seven independent corner-to-corner relations can be described). A non-redundant set of relations can be established by solving (A.5) in terms of the displacement of a given corner point. Choosing corner C1 as a reference point yields the following solution:

$$\begin{aligned} \mathbf{u}_{C2} &= \mathbf{u}_{C1} + \mathbf{a}_2, \\ \mathbf{u}_{C3} &= \mathbf{u}_{C1} + \mathbf{a}_2 + \mathbf{a}_3, \\ \mathbf{u}_{C4} &= \mathbf{u}_{C1} + \mathbf{a}_3, \\ \mathbf{u}_{C5} &= \mathbf{u}_{C1} + \mathbf{a}_1, \\ \mathbf{u}_{C6} &= \mathbf{u}_{C1} + \mathbf{a}_1 + \mathbf{a}_2, \\ \mathbf{u}_{C7} &= \mathbf{u}_{C1} + \mathbf{a}_1 + \mathbf{a}_2 + \mathbf{a}_3, \\ \mathbf{u}_{C8} &= \mathbf{u}_{C1} + \mathbf{a}_1 + \mathbf{a}_3. \end{aligned} \quad (\text{A.6})$$

Observe that the value of the displacement  $\mathbf{u}_{C1}$  of corner C1 can be chosen arbitrarily as the material response is invariant under a rigid body translation. Consequently, choosing  $\mathbf{u}_{C1} = \mathbf{0}$ , the displacements of all corner points can be obtained from (A.6).

For the edges of the cube, Eqs. (A.4) are used again to write 12 displacement constraints between periodic edges. The resulting system has a rank deficiency of three (only nine independent edge-to-edge relations can be described). One possible solution is to solve the system in terms of  $\mathbf{u}_{E7}, \mathbf{u}_{E8}$  and  $\mathbf{u}_{E9}$ , the displacement fields of points along edges E7, E8 and E9, respectively, see Fig. A.10. This yields the following set of relations for the edges of the cube:

$$\begin{aligned}
 \mathbf{u}_{E1} &= \mathbf{u}_{E7} + \mathbf{a}_1 - \mathbf{a}_3, \\
 \mathbf{u}_{E2} &= \mathbf{u}_{E8} + \mathbf{a}_2 - \mathbf{a}_3, \\
 \mathbf{u}_{E3} &= \mathbf{u}_{E7} - \mathbf{a}_3, \\
 \mathbf{u}_{E4} &= \mathbf{u}_{E8} - \mathbf{a}_3, \\
 \mathbf{u}_{E5} &= \mathbf{u}_{E7} + \mathbf{a}_1, \\
 \mathbf{u}_{E6} &= \mathbf{u}_{E8} + \mathbf{a}_2, \\
 \mathbf{u}_{E10} &= \mathbf{u}_{E9} + \mathbf{a}_2, \\
 \mathbf{u}_{E11} &= \mathbf{u}_{E9} + \mathbf{a}_2 - \mathbf{a}_1, \\
 \mathbf{u}_{E12} &= \mathbf{u}_{E9} - \mathbf{a}_1.
 \end{aligned} \tag{A.7}$$

In summary, a set of non-redundant periodic boundary conditions may be prescribed using Eqs. (A.6) to fully specify the displacements of the corner points, Eqs. (A.7) to constrain the displacements of points on the edges (excluding corner points) and finally Eqs. (A.4) to constrain the displacements of points on the external faces (excluding the edges).

## References

- [1] K. Sugimoto, N. Usui, M. Kobayashi, S. Hashimoto, *ISIJ Int.* 32 (1992) 1311–1318.
- [2] B.V.N. Rao, M.S. Rashid, *Mater. Charact.* 39 (1997) 435–453.
- [3] P.J. Jacques, J. Ladrière, F. Delannay, *Metall. Mater. Trans. A* 32 (2001) 2759–2768.
- [4] E.C. Oliver, P.J. Withers, M.R. Daymond, S. Ueta, T. Mori, *Appl. Phys. A* 74 (2002) S1143–S1145.
- [5] S. Zaeferrer, J. Ohlert, W. Bleck, *Acta Mater.* 52 (2004) 2765–2778.
- [6] P.J. Jacques, Q. Furnémont, S. Godet, T. Pardoën, K.T. Conlon, F. Delannay, *Philos. Mag.* 86 (2006) 2371–2392.
- [7] R. Blondé, E. Jimenez-Melero, L. Zhao, J. Wright, E. Brücker, S. van der Zwaag, *N. van Dijk, Acta Mater.* 60 (2012) 565–577.
- [8] G.B. Olson, M. Cohen, *Metall. Trans. A* 6 (1975) 791–795.
- [9] J.B. Leblond, G. Mottet, J.C. Devaux, *J. Mech. Phys. Solids* 34 (1986) 395–409.
- [10] J.B. Leblond, G. Mottet, J.C. Devaux, *J. Mech. Phys. Solids* 34 (1986) 411–432.
- [11] R.G. Stringfellow, D.M. Parks, G.B. Olson, *Acta Metall. Mater.* 40 (1992) 1703–1716.
- [12] F. Marketz, F.D. Fischer, *Model. Simul. Mater. Sci. Eng.* 2 (1994) 1017–1046.
- [13] A. Idesman, V. Levitas, E. Stein, *Comput. Methods Appl. Mech. Eng.* 173 (1999) 71–98.
- [14] M. Cherkaoui, M. Berveiller, *Smart Mater. Struct.* 9 (2000) 592–603.
- [15] S. Turteltaub, A.S.J. Suiker, *J. Mech. Phys. Solids* 53 (2005) 1747–1788.
- [16] A.S.J. Suiker, S. Turteltaub, *Int. J. Numer. Methods Eng.* 63 (2005) 1655–1693.
- [17] S. Turteltaub, A.S.J. Suiker, *Int. J. Solids Struct.* 43 (2006) 4509–4545.
- [18] I. Papatriantafillou, M. Agoras, N. Aravas, G. Haidemenopoulos, *Comput. Methods Appl. Mech. Eng.* 195 (2006) 5094–5114.
- [19] F. Lani, Q. Furnmont, T. Van Rompaey, F. Delannay, P.J. Jacques, T. Pardoën, *Acta Mater.* 55 (2007) 3695–3705.
- [20] L. Delannay, P.J. Jacques, T. Pardoën, *Int. J. Solids Struct.* 45 (2008) 1825–1843.
- [21] V.G. Kouznetsova, M.G.D. Geers, *Mech. Mater.* 40 (2008) 641–657.
- [22] T. Bartel, A. Menzel, B. Svendsen, *J. Mech. Phys. Solids* 59 (2011) 1004–1019.
- [23] R. Mahnken, M. Wolff, C. Cheng, *Int. J. Solids Struct.* 50 (2013) 3045–3066.
- [24] A. Basuki, E. Aernoudt, *J. Mater. Process. Technol.* 89–90 (1999) 37–43.
- [25] B. Verlinden, J. Driver, I. Samajdar, R.D. Doherty, in: R.W. Cahn. (Ed.), *Thermo-Mechanical Processing of Metallic Materials*, vol. 11 of Pergamon Materials Series, Pergamon, 2007, pp. 405–448.
- [26] D.D. Tjahjanto, A.S.J. Suiker, S. Turteltaub, P.E.J. Rivera Diaz del Castillo, S. van der Zwaag, *Comput. Mater. Sci.* 41 (2007) 107–116.
- [27] S. Turteltaub, A.S.J. Suiker, *Int. J. Solids Struct.* 43 (2006) 7322–7336.
- [28] J. Shi, S. Turteltaub, E. Van Der Giessen, *J. Mech. Phys. Solids* 58 (2010) 1863–1878.
- [29] C.H. Seo, K. Kwon, K. Choi, K.H. Kim, J.H. Kwak, S. Lee, N.J. Kim, *Scripta Mater.* 66 (2012) 519–522.
- [30] R.A. Grange, *Metall. Trans.* 2 (1971) 417–426.
- [31] J.A. Charles, *Mater. Sci. Technol.* 14 (1998) 496–503.
- [32] C.C. Tasan, J.P.M. Hoefnagels, M.G.D. Geers, *Scripta Mater.* 62 (2010) 835–838.
- [33] J. Shi, S. Turteltaub, E. Van der Giessen, *Model. Simul. Mater. Sci. Eng.* 19 (2011) [Article No. 074006].
- [34] D.D. Tjahjanto, S. Turteltaub, A.S.J. Suiker, *Continuum Mech. Therm.* 19 (2008) 399–422.
- [35] S. Yadegari, S. Turteltaub, A.S.J. Suiker, *Mech. Mater.* 53 (2012) 1–14.
- [36] J.M. Ball, R.D. James, *Arch. Rat. Mech. Anal.* 100 (1987) 13–52.
- [37] H.B. Callen, *Thermodynamics and an Introduction to Thermostatistics*, second ed., John Wiley & Sons, 1985.
- [38] B.D. Coleman, W. Noll, *Arch. Rat. Mech. Anal.* 13 (1963) 167–178.
- [39] D.D. Tjahjanto, S. Turteltaub, A.S.J. Suiker, S. van der Zwaag, *Model. Simul. Mater. Sci. Eng.* 14 (2006) 617–636.
- [40] E.J. Mittemeijer, *Fundamentals of Materials Science – The Microstructure–Property Relationship using Metals as Model Systems*, 1st ed., Springer, 2011.
- [41] A.S.J. Suiker, S. Turteltaub, *Philos. Mag.* 87 (2007) 5033–5063.
- [42] A.S.J. Suiker, S. Turteltaub, *Model. Simul. Mater. Sci. Eng.* 15 (2007) S147–S166.